Supplementary Information for "Magnetism-induced topological transition in $EuAs_3$"

Erjian Cheng[1,*], Wei Xia[2,3,*], Xianbiao Shi[4,5,*], Chengwei Wang[2,6,*], Chuanying Xi[7], Shaowen Xu[8], Darren C. Peets[9,10], Linshu Wang[1], Hao Su[2], Li Pi[7], Wei Ren[8], Xia Wang[2], Na Yu[2], Yulin Chen[2,3,11], Weiwei Zhao[4,5], Zhongkai Liu[2,3,#], Yanfeng Guo[2,¶], and Shiyan Li[1,12,§]

[1]*State Key Laboratory of Surface Physics, Department of Physics, and Laboratory of Advanced Materials, Fudan University, Shanghai 200433, China*

[2]*School of Physical Science and Technology, ShanghaiTech University, Shanghai 200031, China*

[3]*ShanghaiTech Laboratory for Topological Physics, Shanghai 201210, China*

[4]*State Key Laboratory of Advanced Welding & Joining and Flexible Printed Electronics Technology Center, Harbin Institute of Technology, Shenzhen 518055, China*

[5]*Key Laboratory of Micro-systems and Micro-structures Manufacturing of Ministry of Education, Harbin Institute of Technology, Harbin 150001, China*

[6]*State Key Laboratory of Functional Material for Informatics, Shanghai Institute of Microsystem and Information Technology, Chinese Academy of Sciences, Shanghai 200050, China*

[7]*Anhui Province Key Laboratory of Condensed Matter Physics at Extreme Conditions, High Magnetic Field Laboratory of the Chinese Academy of Sciences, Hefei, Anhui 230031, China*

[8]*Department of Physics, Shanghai University, Shanghai 200444, China*

[9]*Ningbo Institute of Materials Technology and Engineering, Chinese Academy of Sciences, Ningbo, Zhejiang 315201, China*

[10]*Institute for Solid State and Materials Physics, Technical University of Dresden, 01062 Dresden, Germany*

[11]*Department of Physics, University of Oxford, Oxford, OX1 3PU, United Kingdom*

[12]*Collaborative Innovation Center of Advanced Microstructures, Nanjing 210093, China*

I. METHODS

1. Sample synthesis

Eu (99.95%, Alfa Aesar), As (99.999%, PrMat) and Bi (99.9999%, Aladdin) blocks were mixed in a molar ratio of 1:3:26 and placed into an alumina crucible. The crucible was sealed in a quartz ampoule under vacuum and subsequently heated to 900 °C in 15 h. After reaction at this temperature for 20 h, the ampoule was cooled to 700 °C over 20 h, and then slowly cooled to 450 °C at -1 °C/h. The excess Bi flux was then removed using a centrifuge, revealing $EuAs_3$ single crystals with black shiny metallic lustre.

2. Electrical transport and thermodynamic measurements

For electrical transport measurements, a single crystal was cut into a bar shape. A standard four-probe method was used for the longitudinal resistivity measurement. Data were collected in a ^{3}He and a ^{4}He cryostat. Magnetic susceptibility and specific heat measurements were performed in a magnetic property measurement system (MPMS, Quantum Design) and a physical property measurement system (PPMS, Quantum Design), respectively. High-field measurements were performed at the Steady High Magnetic Field Facilities, High Magnetic Field Laboratory, Chinese Academy of Sciences, in Hefei.

3. Angle-resolved photoemission spectroscopy (ARPES) measurements

ARPES measurements were performed at beamline BL13U at the National Synchrotron Radiation Laboratory (NSRL), China (photon energy $h\nu = 12^{-38}$ eV). The samples were cleaved in situ and measured in ultrahigh vacuum with a base pressure of better than 3.5×10^{-11} mbar, and data were recorded by a Scienta R4000 analyzer with the sample at 18 K. The energy and momentum resolution were 10 meV and 0.2°.

4. Density functional theory (DFT) calculations

First-principles calculations were carried out within the framework of the projector augmented wave (PAW) method[1,2], and employed the generalized gradient approximation (GGA)[3] with Perdew-Burke-Ernzerhof

(PBE) formula[4], as implemented in the Vienna *ab initio* Simulation Package (VASP)[5]. Two unit cells repeated along the *b* axis were adopted to simulate the antiferromagnetic configuration indicated by neutron diffraction experiment for $EuAs_3$ [6]. The energy cutoff was chosen to be 500 eV. A Γ-centered 8×6×14 Monkhorst-Pack *k*-point grid was used to produce the well-converged results for the antiferromagnetic phase. For the spin-polarized and paramagnetic band calculations, the same unit cell was used. Γ-centered 10 × 10 × 10 and 6 × 6 × 6 grids were used in the first Brillouin zone for the unit cell and supercell magnetic structures, respectively. The convergence criterion of energy in relaxation was set to be 10^{-6} eV and the atomic positions were fully relaxed until the maximum force on each atom was less than 0.02 eV/Å. The electronic correlations of Eu-4*f* states were treated by the GGA + *U* method[7]. SOC was considered in a self-consistent manner. The Wannier90 package[8] was adopted to construct Wannier functions from the first-principles results. The WannierTools code[9] was used to investigate the topological features of surface state spectra.

II. EXTENDED DATA

1. X-ray diffraction and thermodynamic measurements

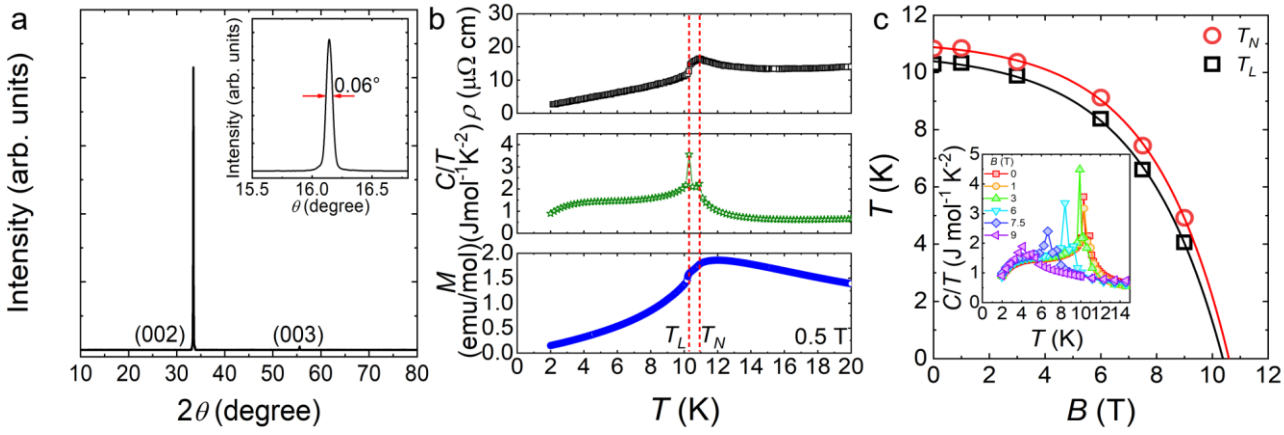

Fig. S1. Basic physical properties of the as-grown $EuAs_3$ single crystals. a, X-ray diffraction pattern from the largest surface of a $EuAs_3$ single crystal. The inset shows the rocking curve of the (002) peak. **b,** Antiferromagnetic (T_N) and lock-in (T_L) transitions demonstrated by resistivity, specific heat and

magnetic susceptibility. **c,** Specific heat measurements under magnetic fields applied along the *c* axis.

Figure S1(a) shows the powder x-ray diffraction (XRD) pattern from the largest surface of a $EuAs_3$ single crystal. The inset shows the x-ray rocking curve of the (002) peak, the full width at half maximum (FWHM) of which is 0.06°, indicative of the high quality of our single crystals. Figure S1(b) shows the verification of the magnetic transitions by resistivity, specific heat and magnetic susceptibility, evidencing the antiferromagnetic (T_N) and lock-in (T_L) transitions at 11 and 10.3 K, respectively, consistent with previous reports[6]. Inset to Fig. S1(c) displays specific heat measurements under magnetic fields. With increasing field, both T_N and T_L decrease. By extrapolating the data to zero temperature, as plotted in Fig. S1(c), T_N and T_L will disappear at $\sim$11.1 and $\sim$10.7 T, respectively. To avoid any influence from the metamagnetic transition and investigate the fully spin-polarized state, we collected our quantum oscillation data above 11.1 T (Figs. 3(b) and 3(e) in the main text).

2. Angular-resolved magnetoresistance (AMR) in low magnetic field

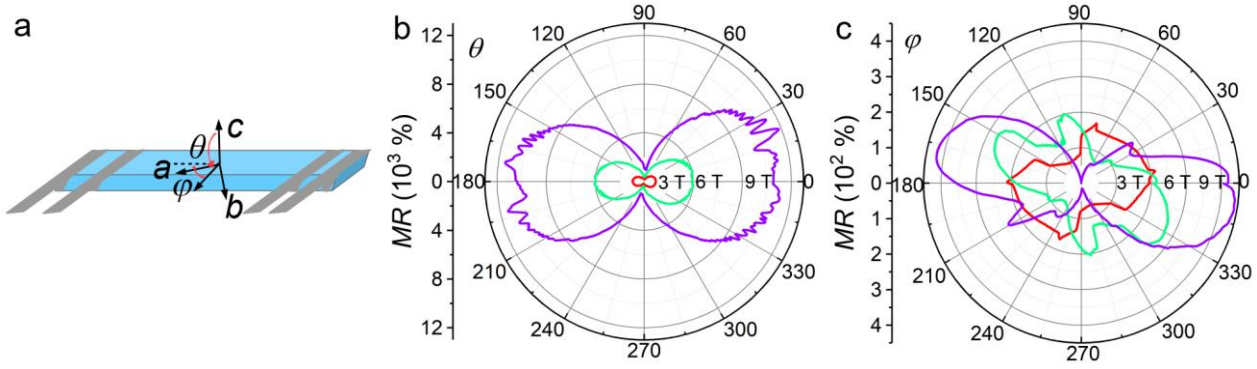

Fig. S2. Angular-resolved magnetoresistance (AMR) of $EuAs_3$ single crystal at 2 K. a, Schematic illustration of the experimental geometry and the angles θ and φ, and polar plots of the AMR for (**b**) θ and (**c**) φ at several magnetic fields.

Figure S2(a) illustrates the experimental geometry for our AMR measurements. For θ = 0° and 90°, the magnetic field is parallel to the *c* axis and the [110] direction, respectively. For φ = 0°, the magnetic field is

parallel to the [110] direction in the *ab* plane, i.e., perpendicular to the electric current *I*. For φ = 90°, the magnetic field is parallel to the electric current *I*. Polar plots of the AMR for θ and φ at several magnetic fields are displayed in Figs. S2(b) and S2(c), respectively, showing typical twofold anisotropy. Compared with θ, the AMR for φ is much more complicated, which is ascribed to the field-induced magnetic transitions[10]. For $\varphi \sim 90°$, i.e., magnetic field parallel to electric current *I*, a negative MR is observed. According to Figs. S2(b) and S2(c), the scenario that external magnetic field suppresses the inelastic magnetic scattering from local moments or magnetic impurities and then induces a negative MR along all directions can be excluded.

3. Band structure in the spin-polarized state

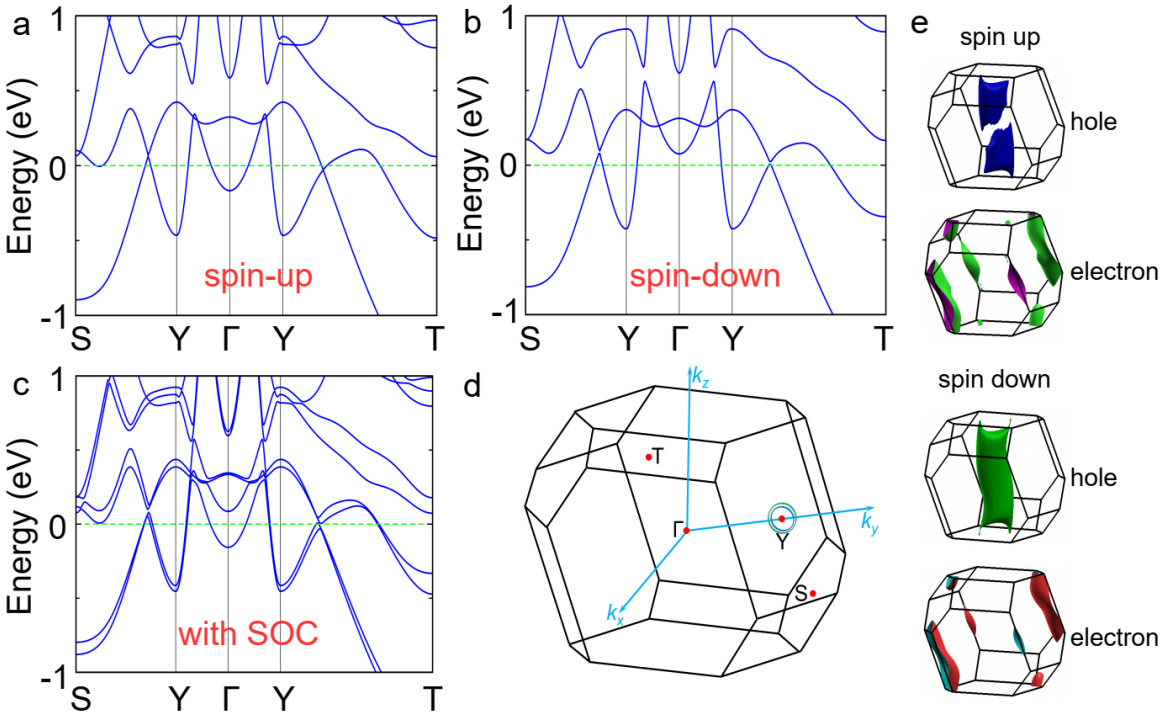

Fig. S3. Topological nodal-line structure in the spin-polarized state of $EuAs_3$. Band calculations for the spin-polarized state of $EuAs_3$: (**a**) spin-up, (**b**) spin-down and (**c**) spin-orbit coupling (SOC)-involved band structures. **d,** The bulk Brillouin zone of spin-polarized $EuAs_3$. The green and blue loops surrounding the *Y* point represent the nodal-line structure for the spin-up and spin-down channels, respectively. **e,** Fermi surfaces of spin-polarized $EuAs_3$.

The GGA+U (U = 5 eV) band structures of the spin-up and spin-down electrons, shown in Figs. 3(a) and 3(b), exhibit topological semimetal states with band crossings near the Fermi level. For both spin-up and spin-down channels, the band crossings persist along a closed path around the Y point in the BZ, showing a double nodal-line structure, as sketched in Fig. S3(d). When spin-orbit coupling (SOC) is considered, the band crossings will be fully gapped because of the band hybridization, as shown in Fig. S3(c). Figure 3(e) shows the Fermi surfaces of the spin-polarized $EuAs_3$ in presence of SOC. There are four main Fermi surface sheets—two hole sheets and two electron sheets. All these Fermi surfaces clearly display three-dimensional (3D) character.

4. Band structure in the paramagnetic state

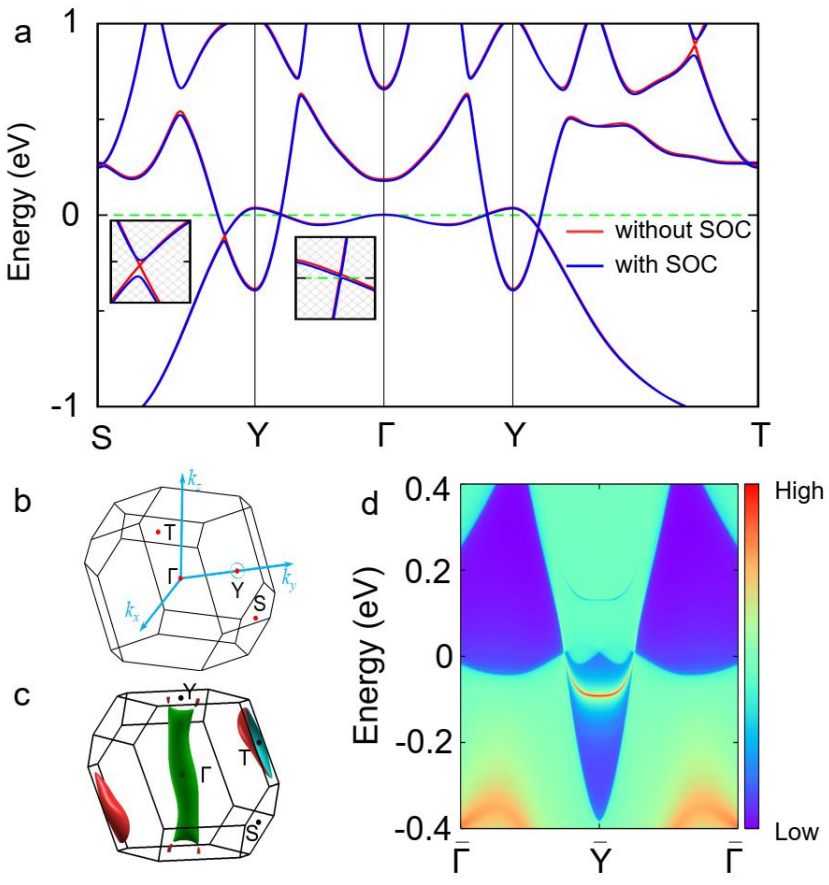

Fig. S4. Topological nodal-line structure in the paramagnetic state of $EuAs_3$. a, Band structure of $EuAs_3$. **b,** The bulk Brillouin zone of the paramagnetic $EuAs_3$. A single nodal loop surrounding the Y point can be seen. **c,** Fermi surface of paramagnetic $EuAs_3$. **d,** The surface states of paramagnetic $EuAs_3$ on

the projected surface perpendicular to the k_z axis.

In order to simulate the paramagnetic phase of $EuAs_3$, we treated the 4*f* electrons on Eu as core electrons. In the absence of SOC, the overall band profiles near the Fermi level, shown in Fig. S4(a), share many key characteristics with those of $SrAs_3$ [11,12], making $EuAs_3$ a topological nodal-line semimetal (TNLS) in the paramagnetic state. Our band structure calculations indicate a nodal loop around the *Y* point in the BZ. When SOC is taken into consideration, gaps will be opened along the nodal line, and $EuAs_3$ becomes a small-gap insulator defined on curved Fermi levels. The calculated surface states in Fig. S4(d) illustrate a drumhead-like surface band, confirming further the TNLS character of paramagnetic $EuAs_3$. The Fermi surface in the paramagnetic state is calculated and displayed in Fig. S4(c), and consists of two large sheets around the Γ and *T* points, and one small sheet around the *Y* point. The Fermi surface in the paramagnetic phase of $EuAs_3$ is very similar in shape to that of $SrAs_3$ [12], indicating that the nodal-line structure is quite robust, so direct verification of the nodal-line structure in the paramagnetic state by ARPES would serve as strong evidence for the existence of the nodal-line structure in the spin-polarized state.

5. Quantum oscillations in the Hall resistivity

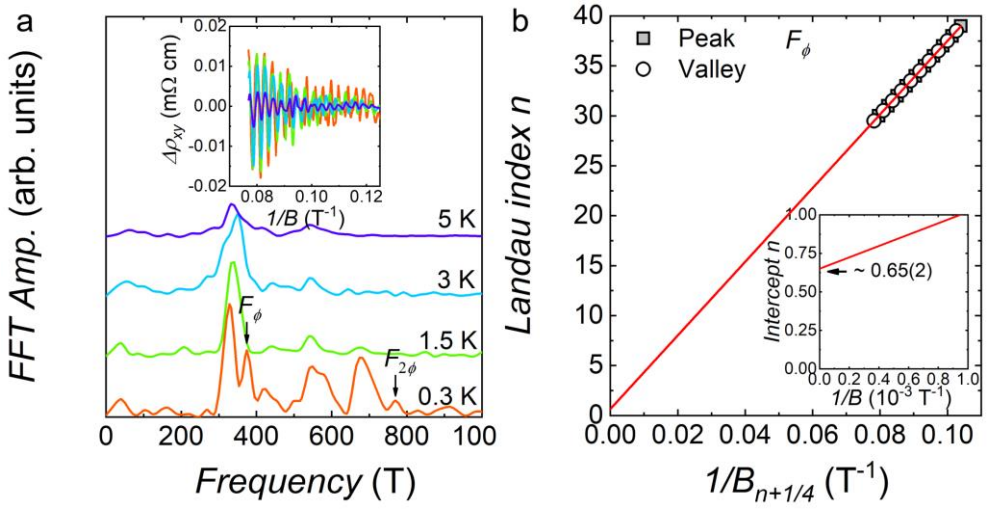

Fig. S5. The analysis of Hall resistivity oscillations of $EuAs_3$ single crystal. a, FFT results based on Hall resistivity oscillations at several temperatures. The inset shows the oscillatory component of ρ_{xy} as a

function of 1/*B*. A new frequency denoted as F_ϕ identifies a new ϕ band. **b,** Landau index *n* as a function of $1/B_{n+1/4}$ in consideration of a 1/4 phase shift[13]. The red line represents a linear fit. The inset shows the extrapolation of 1/*B* to zero.

To check the temperature-induced Lifshitz transition, we analyze the oscillatory component ($\Delta\rho_{xy}$) (displayed in the inset to Fig. S5(a)) via FFT, and a new band (denoted as ϕ) with oscillation frequency of 374 T has been identified, demonstrating the Lifshitz transition. We then check the topology of the φ band, as plotted in Fig. S5(b). We assign integer indices to the $\Delta\rho_{xy}$ peak positions in $1/B_{n+1/4}$ and half integer indices to the $\Delta\rho_{xy}$ valleys, where n+1/4 means the 1/4 phase shift in Hall resistivity compared with longitudinal resistivity[13]. The intercept of 0.65(2) falls in the range between 3/8 and 5/8, as shown in the inset to Fig. 4(d), suggesting the possibly trivial topology of the ϕ band.

6. Possible ferromagnetic fluctuations

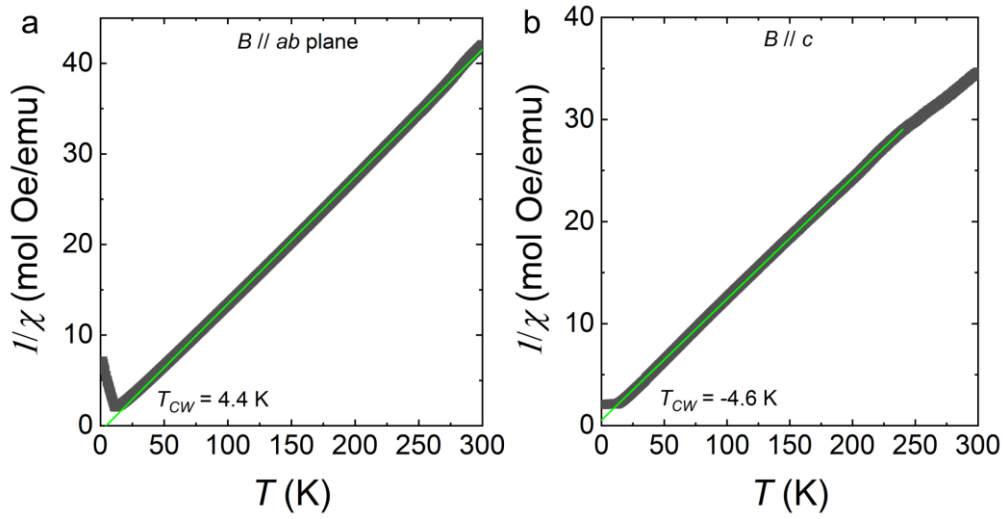

Fig. S6. Temperature dependence of the inverse susceptibility of $EuAs_3$ single crystal. Magnetic fields were applied (**a**) in the *ab* plane, and (**b**) parallel to the *c* axis.

To check whether ferromagnetic correlations exist in the paramagnetic state, the Curie-Weiss temperature T_{CW} is extracted by fitting the temperature dependence of the inverse susceptibility to the Curie-Weiss law,

as shown in Fig. S6. A positive value of 4.4 K is extracted for magnetic fields applied in the *ab* plane, evidencing possible ferromagnetic fluctuations.

7. Exclusion of the open-orbit effect for XMR

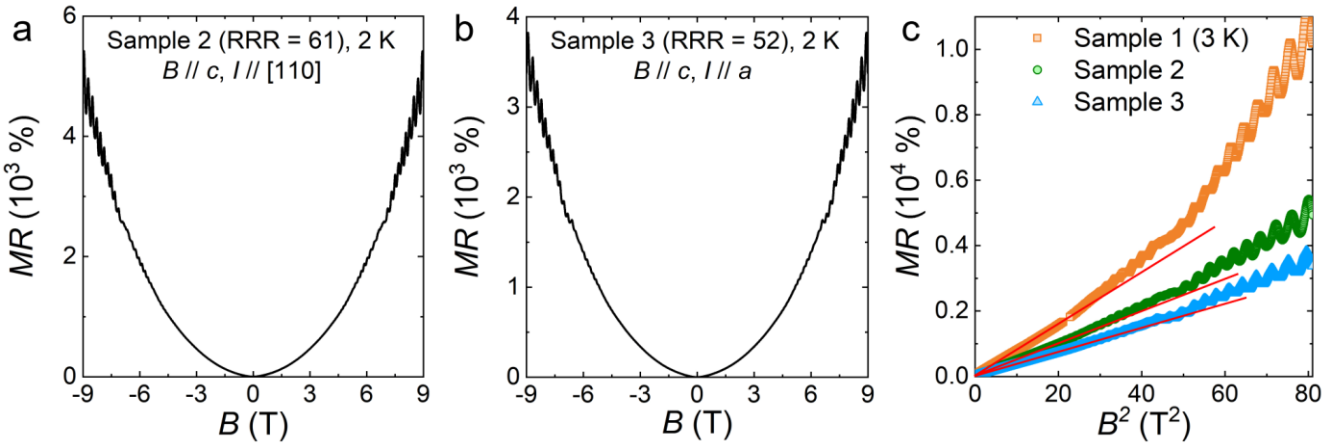

Fig. S7. Magnetoresistance (MR) measurements of $EuAs_3$ single crystal at 2 K with different current direction. a, For Sample 2, magnetic field is applied along the *c* axis, and electric current *I* along the [110] direction. **b,** For Sample 3, magnetic field is applied along the *c* axis, and electric current *I* along the *a* axis. **c,** B^2 as a function of MR for three different samples. The data for Sample 1 is taken from that in Fig. 2(b). With changing the direction of electric current, the unsaturated XMR persists, excluding the open-orbit effect[14].

To exclude the open-orbit effect which may also induce the XMR in $EuAs_3$, we performed the MR measurements with electric current *I* applied along different crystallographic axis, as shown in Fig. S7. Figure S7(a) shows the MR of Sample 2 with magnetic field parallel to *c* axis and electric current applied along the [110] direction, which is the same as Sample 1 (Fig. 2(b)). Compared with Sample 1, the MR of Sample 2 with RRR $\sim$61 is smaller than that of Sample 1, indicating that the quality of single crystal may have a great effect on the magnitude of MR. For Sample 3 with smaller RRR $\sim$52, the MR is smaller than those of Sample 1 and Sample 2. For comparison, we plot the B_2 dependence of MR for these three samples, as shown in Fig. S7(c), which displays similar behavior in spite of the magnitude of MR (The difference

may come from the different quality of single crystals.). According to the open-orbit effect, the unsaturated XMR is only observed for current along the open orbits, which means that changing the current direction will lead to a saturated MR[14]. Therefore, the unsaturated XMR with different current direction in $EuAs_3$ suggests that the XMR resulting from the open-orbit effect can be excluded.

Supplementary References

1. Blöchl, P. E. Projector augmented-wave method. *Phys. Rev. B* **50**, 17953 (1994).

2. Lehtomäki, J. *et al.* Orbital-free density functional theory implementation with the projector augmented-wave method. *J. Chem. Phys.* **141**, 234102 (2014).

3. Perdew, J. P. and Wang, Y. Accurate and simple analytic representation of the electron-gas correlation energy. *Phys. Rev. B* **4**, 13244 (1992).

4. Perdew, J. P., Burke, K. and Ernzerhof, M. Generalized gradient approximation made simple. *Phys. Rev. Lett.* **77**, 3865 (1996).

5. Kresse, G. and Furthmller, J. Efficiency of *ab-initio* total energy calculations for metals and semiconductors using a plane-wave basis set. *Comput. Mater. Sci.* **6**,15-50 (1996).

6. Chattopadhyay, T., Schnering, H. G. v. and Brown, P. J. Neutron diffraction study of the magnetic ordering in $EuAs_3$. *J. Magn. Magn. Mater.* **28**, 247-249 (1982).

7. Anisimov, V. I., Aryasetiawan, F. and Lichtenstein, A. I. First-principles calculations of the electronic structure and spectra of strongly correlated systems: the LDA+*U* method. *J. Phys. Condens. Matter.* **9**, 767 (1997).

8. Marzari, N. and Vanderbilt, D. Maximally localized generalized Wannier functions for composite energy bands. *Phys. Rev. B* **56**, 12847 (1997).

9. Wang, Q. S. *et al.* WannierTools: An open-source software package for novel topological materials. *Comput. Phys. Commun.* **224**, 405-416 (2018).

10 Bauhofer, W. and McEwer, K. A. Anisotropic magnetoresistance of the semimetallic antiferromagnet $EuAs_3$. *Phys. Rev. B* **43**, 13450-13455 (1991).

11. Xu, Q. *et al.* Topological nodal line semimetals in CaP_3 family of materials. *Phys. Rev. B* **95**, 045136 (2017).

12. Li, S. C. *et al.* Evidence for a Dirac nodal-line semimetal in $SrAs_3$. *Sci. Bull.* **63**, 535-541 (2018).

13. He, L. P. *et al.* Quantum Transport Evidence for the Three-Dimensional Dirac Semimetal Phase in Cd_3As_2. *Phys. Rev. Lett.* **113**, 246402 (2014).

14. Zhang, S. N. *et al.* Magnetoresistance from Fermi surface topology. *Phys. Rev. B* **99**, 035142 (2019).